GAS STORAGE

Balancing volumetric and gravimetric uptake in highly porous materials for clean energy

Zhijie Chen[1]*, Penghao Li[1]*, Ryther Anderson[2]*, Xingjie Wang[1], Xuan Zhang[1], Lee Robison[1], Louis R. Redfern[1], Shinya Moribe[1,3], Timur Islamoglu[1], Diego A. Gómez-Gualdrón[2], Taner Yildirim[4], J. Fraser Stoddart[1,5,6], Omar K. Farha[1,7]†

A huge challenge facing scientists is the development of adsorbent materials that exhibit ultrahigh porosity but maintain balance between gravimetric and volumetric surface areas for the onboard storage of hydrogen and methane gas—alternatives to conventional fossil fuels. Here we report the simulation-motivated synthesis of ultraporous metal–organic frameworks (MOFs) based on metal trinuclear clusters, namely, NU-1501-M (M = Al or Fe). Relative to other ultraporous MOFs, NU-1501-Al exhibits concurrently a high gravimetric Brunauer–Emmett–Teller (BET) area of 7310 $m^2\ g^{-1}$ and a volumetric BET area of 2060 $m^2\ cm^{-3}$ while satisfying the four BET consistency criteria. The high porosity and surface area of this MOF yielded impressive gravimetric and volumetric storage performances for hydrogen and methane: NU-1501-Al surpasses the gravimetric methane storage U.S. Department of Energy target (0.5 g g^{-1}) with an uptake of 0.66 g g^{-1} [262 cm^3 (standard temperature and pressure, STP) cm^{-3}] at 100 bar/270 K and a 5- to 100-bar working capacity of 0.60 g g^{-1} [238 cm^3 (STP) cm^{-3}] at 270 K; it also shows one of the best deliverable hydrogen capacities (14.0 weight %, 46.2 g $liter^{-1}$) under a combined temperature and pressure swing (77 K/100 bar → 160 K/5 bar).

In 2017, for the first time in history, the U.S. petroleum-based transportation sector, which includes cars, trucks, planes, trains, and boats, overtook power plants as the largest source of greenhouse gas emissions in the country (*1*). This progression continued in 2018 as the transportation sector emitted 1.86 billion metric tons of CO_2 and power plants emitted 1.76 billion metric tons of CO_2, and this trend is projected to continue (*1*). This shift in CO_2 emissions makes finding alternative sources of cleaner energy for transportation even more important and judicious.

Methane and hydrogen are both alternatives to gasoline for potential use as fuel for the transportation sector (*2*, *3*). Methane is envisioned as a transitional fuel, as its combustion still emits CO_2, but the amount of CO_2 released is less than that of gasoline (*4*). Hydrogen, by contrast, is envisioned as the "fuel of the future," as hydrogen-powered fuel cell vehicles are zero-emission automobiles (*2*). However, the transportation, storage, and operations of hydrogen- and methane-powered vehicles currently require high-pressure compression (i.e., 700 bar for H_2 and 250 bar for CH_4), which is both costly and potentially unsafe (*2*, *5*). To encourage research in this important field, the U.S. Department of Energy (DOE) established metrics for the development of onboard storage and delivery systems for alternative fuels for the transportation sector (*2*, *6*). For methane, these targets include a gravimetric storage capacity of 0.5 g g^{-1} and a volumetric storage capacity of 263 cm^3 (standard temperature and pressure, STP) cm^{-3}. For hydrogen, these targets (for 2020) include a gravimetric storage capacity of 4.5 weight (wt) % and a volumetric storage capacity of 30 g $liter^{-1}$.

Developing new adsorbent materials is one of the strategies to reach these targets for the safe and cost-effective storage of methane and hydrogen. In particular, high–surface area porous materials (*3*, *7*–*9*)—often thought of as having a surface area of 2000 m^2/g or greater—such as metal–organic frameworks (MOFs) (*3*, *5*, *8*, *10*–*16*), porous carbons (*5*, *17*), covalent organic frameworks (*18*), and porous organic polymers (*19*–*22*) have been investigated intensively as candidate adsorbents for the onboard storage of clean-energy gases. The properties of these adsorbents could enable gas loadings to power vehicles under less extreme loading pressure (e.g., 100 bar) than that currently needed by the storage systems used in methane- and hydrogen-powered vehicles. Among these adsorbents, MOFs, constructed from inorganic nodes and organic linkers, have gained prominence as appealing materials for gas storage (*23*–*27*) because of their tailorable pore chemistry, pore geometry, and amenability for rational design, facilitated by clear-cut structure-property relationships. Furthermore, surface areas in MOFs have been reported to reach ultrahigh values (*28*–*30*).

When these adsorbents are used, the tank pressure goes down as fuel is consumed until there is no longer a gradient driving the flow of methane or hydrogen to the engine, which typically occurs at 5 bar (*2*, *26*). At this pressure, a substantial fraction of gas may still be adsorbed. Therefore, the deliverable capacity—the amount of stored gas delivered to the engine during operation—becomes a critical design parameter when designing adsorbents. The deliverable capacity for the 100 bar → 5 bar pressure swing has received exceptional interest because 100 bar is the highest refueling pressure for which all-metal Type I pressure tanks can be safety-compliant, circumventing the need for more expensive carbon fiber–reinforced composite vessels for hydrogen storage (*2*, *31*). As both size and weight requirements for the onboard tank must be met to make the storage system feasible, it is crucial to consider the optimization of volumetric and gravimetric deliverable capacities in MOFs as concurrent objectives rather than separate ones (*13*, *32*–*34*).

As the existence of a trade-off between gravimetric and volumetric capacities has become apparent (*33*), there is a great challenge in providing satisfactory volumetric and gravimetric capacities within a single material. For example, microporous HKUST-1 (*5*, *35*), with a relatively low gravimetric Brunauer–Emmett–Teller (BET) area of 1980 $m^2\ g^{-1}$ (a volumetric BET area of 1740 $m^2\ cm^{-3}$), exhibits high volumetric storage but moderate gravimetric CH_4 uptake [281 cm^3 (STP) cm^{-3} and 0.23 g g^{-1} at 100 bar/ 298 K], whereas mesoporous MOF-210 (*7*), with a comparatively high gravimetric BET area of 6240 $m^2\ g^{-1}$ (a volumetric BET area of 1560 $m^2\ cm^{-3}$), shows high gravimetric storage capacity yet low volumetric CH_4 uptake [0.48 g g^{-1} and 168 cm^3 (STP) cm^{-3} at 80 bar/ 298 K]. Typically, ultraporous MOF materials—i.e., MOF-210 (*7*), NU-110 (*28*), and DUT-60 (*30*)—with high gravimetric BET areas, though containing high pore volumes and large pore sizes, show relatively low volumetric areas, which limits their applications in gas storage that requires a balance of volumetric and gravimetric capacities. Clearly, one key step toward a satisfactory trade-off between volumetric and gravimetric capacities would be to impart a single material with both high volumetric and gravimetric surface areas.

Results and discussion

To pursue both high gravimetric and volumetric surface areas in a single material, we used NU-1500 (*36*) as a starting point (Fig. 1). This class of material has several appealing characteristics, including (i) high porosity and surface area with a relatively small pore size of ~1.4 nm; (ii) a broad degree of designability—the combination of rigid trigonal prismatic linkers

[1]Department of Chemistry and International Institute for Nanotechnology, Northwestern University, 2145 Sheridan Road, Evanston, IL 60208, USA. [2]Department of Chemical and Biological Engineering, Colorado School of Mines, Golden, CO 80401, USA. [3]Future Mobility Research Department, Toyota Research Institute of North America, Ann Arbor, Michigan 48105, USA. [4]NIST Center for Neutron Research, National Institute of Standards and Technology, Gaithersburg, MD 20899, USA. [5]Institute for Molecular Design and Synthesis, Tianjin University, 92 Weijin Road, Tianjin 300072, China. [6]School of Chemistry, University of New South Wales, Sydney, NSW 2052, Australia. [7]Department of Chemical and Biological Engineering, Northwestern University, 2145 Sheridan Road, Evanston, IL 60208, USA.
*These authors contributed equally to this work.
†Corresponding author. Email: o-farha@northwestern.edu

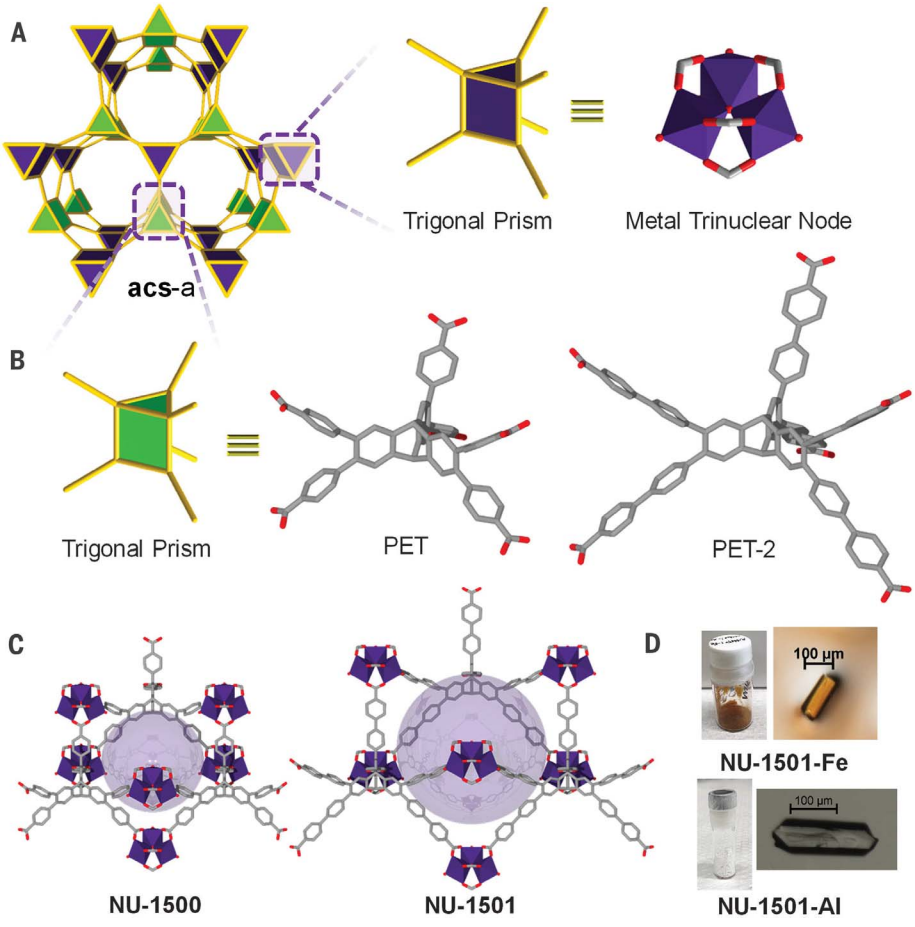

Fig. 1. Design and synthesis of NU-1501. (**A** to **C**) Schematic representation of **NU-1501-M** (M = Fe and Al) with the 6-c **acs** net. Atom color scheme: carbon, Gray; metal polyhedron, Northwestern University (NU) purple; O, red. H atoms are omitted for the sake of clarity. (**D**) Optical images of the single crystals of NU-1501.

and M_3O metal trimers will form MOFs with the **acs** net; (iii) good moisture stability for ease of processing; and finally, (iv) the versality of metal trimers that allow it to be synthesized from M^{3+} metals, including abundant metals such as aluminum and iron. To start, we synthesized a new aluminum MOF, NU-1500-Al, [$Al_3(\mu_3\text{-}O)(H_2O)_2(OH)$(PET)], which exhibits 6-c **acs** topology and has rigid trigonal prismatic triptycene-based organic ligands—i.e., peripherally extended triptycene (*37*) (H_6PET)—and aluminum μ_3-oxo-centered trinuclear clusters (*38*) (figs. S5 and S10). We confirmed the permanent microporosity of activated NU-1500-Al by nitrogen (N_2) adsorption isotherm at 77 K, which exhibited an apparent BET area of 3560 $m^2\ g^{-1}$—satisfying the four BET consistency criteria (*39*, *40*)—and which also had an experimental total pore volume of 1.46 $cm^3\ g^{-1}$, in good agreement with the value for the simulated structure and previously reported (*36*) NU-1500-Fe (figs. S15 to S17). The volumetric BET area of NU-1500-Al is estimated to be ~1770 $m^2\ cm^{-3}$, based on the crystallographic density from the simulated structure. The pore-size distribution from a density functional theory (DFT) model with slit pore geometry revealed one type of pore centered at 1.4 nm, which agrees with the previous values from other NU-1500 analogs (*36*) (fig. S19).

On account of its high micropore volume and surface area, high-pressure H_2 and CH_4 sorption studies were conducted on NU-1500-Al at the National Institute for Standards and Technology (NIST) (figs. S31 to S36). At 100 bar, NU-1500-Al adsorbed ~0.34 g g^{-1} [237 cm^3 (STP) cm^{-3}] and ~0.39 g g^{-1} [273 cm^3 (STP) cm^{-3}] of CH_4 at 296 and 270 K, respectively, with deliverable capacities of ~0.29 g g^{-1} [202 cm^3 (STP) cm^{-3}] and ~0.32 g g^{-1} [224 cm^3 (STP) cm^{-3}] between 5 and 100 bar. The volumetric deliverable capacities of 5 to 100 bar for NU-1500-Al are comparable to those of benchmark methane-storage materials, such as MOF-905 (*25*) [203 cm^3 (STP) cm^{-3}; 5 to 80 bar at 298 K], HKUST-1 (*5*) [207 cm^3 (STP) cm^{-3}; 5 to 100 bar at 298 K], and Al-**soc**-MOF-1 (*13*) [201 cm^3 (STP) cm^{-3}; 5 to 80 bar at 298 K] (table S6). NU-1500-Al adsorbed ~8.6 wt % (46.8 g $liter^{-1}$) of H_2 at 100 bar and 77 K, with a deliverable capacity of 8.2 wt % (44.6 g $liter^{-1}$) under combined temperature and pressure swing conditions: 77 K/100 bar →160 K/5 bar, which agrees with the tank design conditions proposed (*41*) by the DOE (table S7).

Motivated by the results from NU-1500, we first set out to understand the trade-off between gravimetric and volumetric surface area (GSA and VSA, respectively). To accomplish this task, we created a topologically diverse (58 topologies) 2800-MOF database, including 50 MOFs isoreticular to NU-1500, using the ToBaCCo (*42*) code (figs. S50 to S54). Both gravimetric and volumetric surface areas were calculated geometrically for the created structures. Plotting these two quantities against each other (Fig. 2A) reveals their trade-off, which can be quantified by their normalized product (GSA × VSA).

The GSA × VSA product shows a volcano-type relationship between MOF helium void fraction (VF) and largest pore diameter (LPD) (Fig. 2, B and C), with MOFs at the top of the volcano presenting the ideal trade-off (GSA × VSA product in the 95th percentile). The intermediate MOFs in this database that still exhibit these ideal qualities display an average VF of 0.85 and an average LPD of 17.2 Å. By comparison, NU-1500 presents values of 0.76 and 12.7 Å, respectively, indicating opportunities to improve the trade-off by refining the MOF design. Indeed, the obtained structure-property relationships revealed the value of extending the rigid triptycene-based ligand of the NU-1500 by one phenyl ring, going from PET to PET-2 (*43*) (Fig. 1C).

We named the PET-2–based structure "NU-1501" and noticed that it presents properties (VF = 0.87, LPD = 18.8 Å) closer to the average of the MOFs in the ideal trade-off region. Simply meeting either property value does not guarantee an ideal trade-off. For instance, MOFs with "ideal" VFs cover a wide range for the GSA × VSA product. Thus, NU-1501 has other complementary features that boost its GSA × VSA product such as low metal atom–to–organic atom ratio. For example, figs. S51E and S51F show that MOFs with lower metal atom–to–organic atom ratios tend to have higher GSA × VSA products. This is because organic atom moieties (e.g., aromatic rings) tend to provide large adsorption surfaces while being light compared to metals.

To understand the implications of an ideal VSA versus GSA trade-off, we predicted methane and hydrogen deliverable capacities for the MOFs in the database (Fig. 2, D, E and F). Notably, there is broader peak in the gravimetric deliverable capacity (GDC) versus volumetric deliverable capacity (VDC) than in the VSA versus GSA trade-off, meaning that MOFs with maximally high GDC (and thus generally maximally high GSA) are included in the ideal trade-off region. From fig. S54, we see that there are many MOFs within the ideal trade-off region for deliverable capacity that have a GSA too high to

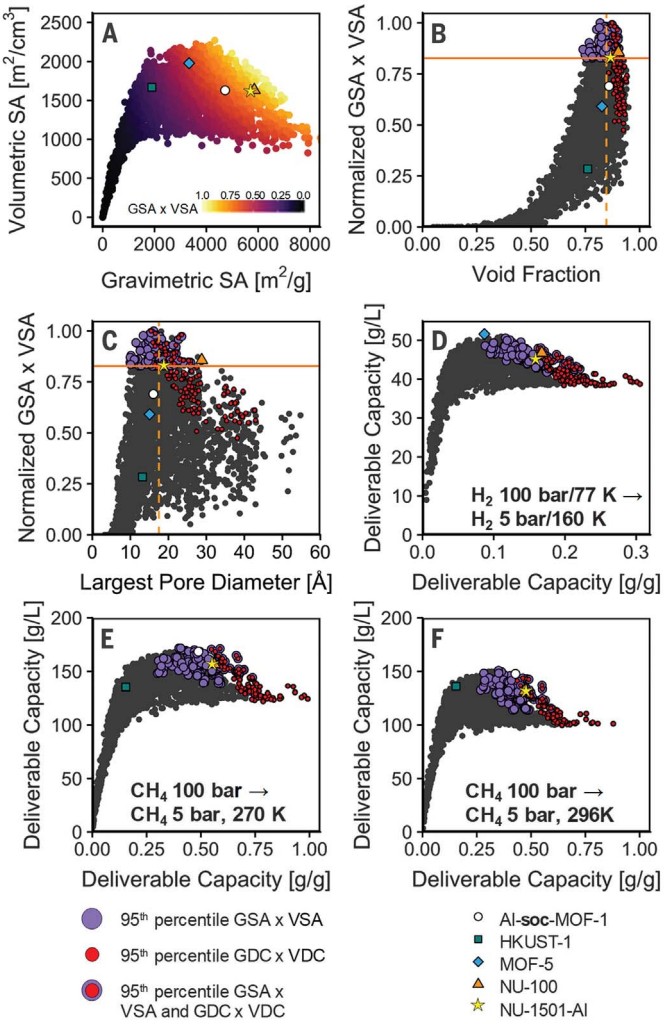

Fig. 2. Trade-offs of gravimetric and volumetric properties predicted by molecular simulation. (**A**) VSA versus GSA, colored by the product of the two. NU-1501-Al lies in the ideal trade-off region, characterized as being just past the peak of volumetric SA. Al-**soc**-MOF-1, HKUST-1, MOF-5, and NU-100 are shown for comparison. (**B**) The product of GSA and VSA versus void fraction. The horizontal orange line shows the cutoff for being in the 95th percentile of GSA × VSA. The dashed, vertical orange line shows the average void fraction for MOFs in the 95th percentile. (**C**) Analogous to (B) except plotting GSA × VSA versus MOF largest pore diameter. (**D**) Volumetric deliverable capacity (VDC) versus gravimetric deliverable capacity (GDC) for hydrogen. Purple points show MOFs in the ideal region (95th percentile of GSA × VSA) of the GSA/VSA trade-off. Red points show MOFs in the 95th percentile of GDC × VDC. Red points outlined in purple show MOFs in both regions. (**E**) Analogous to (D) except for methane VDC and GDC at 270 K. (**F**) Analogous to (D) except for methane VDC and GDC at 296 K.

be in the ideal trade-off region for surface area. NU-1501 lies exactly at the boundary of MOFs in the ideal trade-off region for deliverable capacity and MOFs in the ideal trade-off region for surface area (in all cases), meaning that NU-1501-Al maintains maximally high VSA for MOFs with GDC × VDC in the 95th percentile (whereas most other MOFs have higher GSA and lower VSA).

Inspired by the computational results above, we decided to synthesize expanded versions of **acs**-MOFs—i.e., NU-1501, which features an extended ligand design, H_6PET-2 (figs. S1 to S4). Solvothermal reactions of H_6PET-2 with $AlCl_3{\cdot}6H_2O$ and $FeCl_3{\cdot}6H_2O$ yielded (Fig. 1D) colorless and yellow-orange hexagonal block crystals. Single-crystal x-ray diffraction (SCXRD) studies of these materials (NU-1501-Al and NU-1501-Fe) revealed noncatenated structures crystallizing in a hexagonal space group ($P\bar{6}m2$) (tables S1 and S2). The μ_3-oxo-centered trinuclear metal inorganic clusters are linked by the fully deprotonated trigonal prismatic ligands, H_6PET-2, to yield a 3-periodic **acs**-MOF having one type of open hexagonal channel with a pore size of ~2.2 nm. We predicted the formula to be $[M_3(\mu_3\text{-}O)(H_2O)_2(OH)(PET\text{-}2)]$ (M = Al or Fe), with the terminal anionic groups on the trinuclear node being -OH, as supported by the absence of chloride signals from energy-dispersive x-ray analysis (figs. S11 to S13). We confirmed the phase purities of the bulk NU-1501-Al and NU-1501-Fe, based on similarities (fig. S6) between the simulated and as-synthesized powder x-ray diffraction (PXRD) patterns.

The permanent porosity of NU-1501-Al and NU-1501-Fe after supercritical CO_2 activation has been confirmed by reversible N_2 and Ar adsorption and desorption isotherms at 77 and 87 K, respectively. Both materials have very similar isotherms (Fig. 3 and figs. S18 to S24). The experimental total pore volumes of NU-1501-Al, calculated from the N_2 and Ar adsorption isotherms, are 2.91 and 2.93 $cm^3\ g^{-1}$, respectively, which agree well with the simulated values from the single-crystal structure. The pore-size distribution based on a DFT model revealed that NU-1501-Al has pore sizes ranging from 1.5 to 2.5 nm, with two types of pores centered at ~1.7 and 2.2 nm, which agrees well with the two pores from the single-crystal structure. The apparent BET area of NU-1501-Al based on the N_2 adsorption isotherm is estimated to be 7310 $m^2\ g^{-1}$ after satisfying all four BET consistency criteria (*39*, *40*). If only the first two BET consistency criteria are fulfilled—as in the recently reported (*30*) ultraporous material, DUT-60—the apparent BET area is estimated to reach 9150 $m^2\ g^{-1}$ (table S3). Moreover, the apparent BET area of NU-1501-Al, based on the Ar adsorption isotherm, attains 7920 $m^2\ g^{-1}$ after satisfying the first three BET consistency criteria, which is in line with the simulated BET area of 7760 $m^2\ g^{-1}$ from the simulated Ar adsorption isotherm (table S4). The deviation from the BET criteria should be minimized when it is not possible to select a region fulfilling all four consistency criteria, as in the case of the BET area calculation (*40*) from the Ar adsorption isotherm of NU-1501-Al. To the best of our knowledge, the gravimetric BET area (7310 $m^2\ g^{-1}$) of NU-1501-Al is the highest reported value for all porous materials after satisfying all four BET criteria, despite the pore volume (about 2.90 $cm^3\ g^{-1}$) being lower than those of ultraporous materials having BET areas larger than 7000 $m^2\ g^{-1}$ (table S5). Notably, the volumetric BET area of NU-1501-Al reaches 2060 $m^2\ cm^{-3}$, based on the crystallographic density. This volumetric BET area is among the highest of all reported porous materials with gravimetric BET areas higher than 5000 $m^2\ g^{-1}$, and is much higher than that of similar ultraporous MOFs such as NU-110 (*28*) (1585 $m^2\ cm^{-3}$), MOF-210 (*7*) (1560 $m^2\ cm^{-3}$), and DUT-60 (*30*) (1466 $m^2\ cm^{-3}$). The isotherm is highly reproducible, as illustrated by the similarities of isotherms taken from four different batches at Northwestern University and at NIST (fig. S18).

As revealed by the geometrical calculation of the pore size distribution from the crystal structures (fig. S49), there are two main features that allow NU-1501-Al to maintain a higher volumetric surface area over other MOFs—i.e., MOF-210 (*7*), NU-100 (*8*), NU-110 (*28*), and DUT-60 (*30*)—with similar gravimetric surface areas and higher pore volumes: (i) The largest pore of NU-1501-Al is much smaller than those of MOF-210 (*7*), NU-100 (*8*), NU-110 (*28*), and DUT-60 (*30*); and (ii) NU-1501-Al has only one dominant pore.

The iron-based analog of NU-1501 (NU-1501-Fe) shows gravimetric and volumetric BET areas (7140 $m^2\ g^{-1}$ and 2130 $m^2\ cm^{-3}$) similar to those of the aluminum-based NU-1501 and also features an experimental pore volume (2.90 $cm^3\ g^{-1}$) similar to that of NU-1501-Al, illustrating the versatility of this MOF design and synthetic

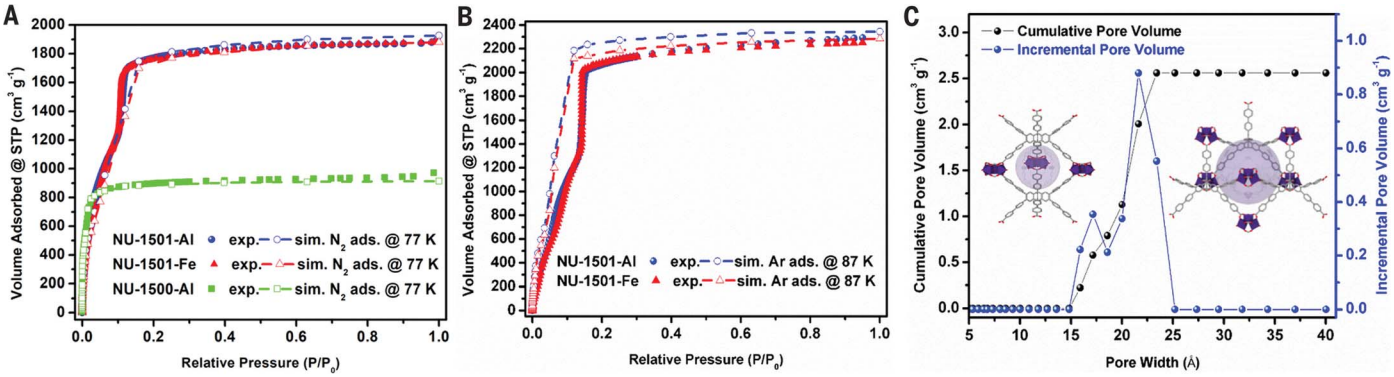

Fig. 3. Porosity measurements of NU-1501. (**A**) Experimental and simulated N_2 (77 K) adsorption isotherms of NU-1501 and NU-1500-Al. (**B**) Experimental and simulated Ar (87 K) adsorption isotherms of NU-1501. (**C**) DFT pore size distribution of NU-1501-Al from N_2 (77 K) adsorption isotherm. The dashed lines are a guide to the eye for simulated data.

strategy (fig. S20). Molecular simulations further revealed that NU-1501-Al and NU-1501-Fe have higher geometric surface areas (5714 and 5513 $m^2 g^{-1}$, respectively), when calculated with the N_2 sized probe, than that of NU-1500-Al (3634 $m^2 g^{-1}$) (table S8). Additionally, the trivalent metal-based trimer (i.e., Al_3O or Fe_3O) of NU-1501 produces a relatively more stable framework than the traditional ultraporous MOFs with BET areas larger than 6000 $m^2 g^{-1}$ based on Zn_4O or copper paddlewheel building units (*7*, *28*, *30*, *36*). The overall stability of NU-1501 was tested by SCXRD, PXRD, and N_2 sorption measurements after soaking in liquid water, and by variable-temperature PXRD studies (table S2 and figs. S7 to S9, S14, and S25 to S27). To this end, NU-1501 represents an ultraporous material balancing both gravimetric and volumetric BET areas simultaneously—i.e., larger than 7000 $m^2 g^{-1}$ and 2000 $m^2 cm^{-3}$—making them promising candidates for clean energy–related gas storage (i.e., H_2 and CH_4).

Considering the exceptional gravimetric and volumetric surface areas, methane and hydrogen high-pressure sorption experiments were performed on activated NU-1501 at NIST (Fig. 4 and figs. S37 to S48). NU-1501-Al displays one of the top gravimetric methane uptakes among MOF materials at 80 bar—0.60 g g^{-1} at 270 K and 0.48 g g^{-1} at 296 K. The 5- to 80-bar methane working capacities of NU-1501-Al are ~0.44 g g^{-1} [174 cm^3 (STP) cm^{-3}; 296 K] and ~0.54 g g^{-1} [214 cm^3 (STP) cm^{-3}; 270 K]. These methane capacities are comparable to those of other MOF materials such as MOF-210 (*7*), Al-**soc**-MOF-1 (*13*), ST-2 (*44*), and MOF-905 (*25*). At room temperature, the gravimetric deliverable methane capacity of NU-1501-Al at working pressure between 80 bar (adsorption) and 5 bar (desorption) is comparatively similar to that of the benchmark Al-**soc**-MOF-1, whereas the volumetric deliverable capacity is slightly lower (Fig. 5). Notably, NU-1501-Al adsorbed ~0.54 g g^{-1} [214 cm^3 (STP) cm^{-3}] and ~0.66 g g^{-1} [262 cm^3 (STP) cm^{-3}] of CH_4 at 100 bar and at 296 and 270 K, respectively. Deliverable capacities between 5 and 100 bar are 0.50 g g^{-1} [198 cm^3 (STP) cm^{-3}; 296 K] and ~0.60 g g^{-1} [238 cm^3 (STP) cm^{-3}; 270 K], suggesting that NU-1501-Al is among the best porous crystalline materials for methane storage (table S6). The uptake capacities of NU-1501-Al surpass the materials-level gravimetric CH_4 storage DOE target (0.5 g g^{-1}) at 100 bar at both room temperature and 270 K (*6*, *9*, *25*). The gravimetric deliverable capacity at 270 K and 5- to 100-bar—i.e., 0.60 g g^{-1}—is even higher than that of the recently reported record MOF materials (table S6). The gravimetric methane uptakes at 100 bar at 296 and 270 K are also much higher than those of the microporous isostructural NU-1500-Al (0.34 g g^{-1} at 296K and 0.39 g g^{-1} at 270 K; at 100 bar), despite similar volumetric uptake [214 versus 237 cm^3 (STP) cm^{-3} at 296 K; 262 versus 273 cm^3 (STP) cm^{-3} at 270 K]. This suggests that the isoreticular extension of NU-1500 to NU-1501 substantially increases gravimetric methane capacity without sacrificing volumetric performance (Fig. 5). Additionally, at near-freezing temperatures, NU-1501-Al shows (Fig. 5F) a higher volumetric 5- to 100-bar deliverable methane capacity than HKUST-1 [238 cm^3 (STP) cm^{-3} at 270 K versus 195 cm^3 (STP) cm^{-3} at 273 K] because of the much lower unused methane uptake at 5 bar while having a considerably better gravimetric 5- to 100-bar deliverable capacity (0.60 g g^{-1} at 270 K versus 0.16 g g^{-1} at 273 K). NU-1501-Fe, compared to NU-1501-Al, adsorbed slightly less CH_4 (~0.52 g g^{-1} at 296 K and ~0.63 g g^{-1} at 270 K; at 100 bar) under the same conditions because of the slightly lower surface area and pore volume (figs. S45 to S48).

The isosteric heats of adsorption (Q_{st}) of NU-1501-Al for CH_4 (figs. S42) were calculated from the isotherms and found to be 9.7 and 10.9 kJ mol^{-1} at low and high loading, respectively. The experimental Q_{st} of NU-1501-Al is close to the enthalpy of adsorption calculated from the grand canonical ensemble Monte Carlo (GCMC) simulations at low pressure—10.3 kJ mol^{-1} (table S9). These data suggest that moderate host–guest interactions occur between the framework and methane gas, which is ideal for achieving high deliverable capacities. The Q_{st} value of NU-1501 is slightly less than that for NU-1500-Al (13.7 kJ mol^{-1}) and is most likely due to the smaller pore size of NU-1500. The simulated adsorption isotherms at various temperatures and pressures closely resemble the experimental isotherms, further validating the successful activation of the materials and the high-pressure adsorption results of NU-1501.

NU-1501-Al and NU-1501-Fe are among the best MOFs for hydrogen storage under combined temperature and pressure swing conditions (77 K/100 bar →160 K/5 bar) (Fig. 5B and table S7) (*33*, *34*, *41*, *45*). H_2 adsorption isotherms revealed that NU-1501-Al adsorbs ~14.5 wt % (47.9 g $liter^{-1}$) of H_2 at 100 bar and 77 K, with a high deliverable capacity of 14.0 wt% (46.2 g $liter^{-1}$) under the conditions 77 K/100 bar →160 K/5 bar. NU-1501-Fe shows a slightly lower deliverable capacity (13.2 wt %; 45.4 g $liter^{-1}$) than NU-1501-Al under the same conditions. The experimental H_2 adsorption isotherms closely match the simulated isotherms at various temperatures, which confirmed the near complete activation of the MOFs. In addition, both the absolute uptake at 77 K/100 bar and the deliverable capacities of NU-1501-Al for H_2 are much higher than those of NU-1500-Al while maintaining nearly identical volumetric uptake and capacities (14.0 versus 8.2 wt % and 46.2 g $liter^{-1}$ versus 44.6 g $liter^{-1}$ under the aforementioned operational condition), further demonstrating the effectiveness of extension of this **acs**-MOF platform in balancing the gravimetric and volumetric performance of H_2 storage. In agreement with the simulated results, the experimental

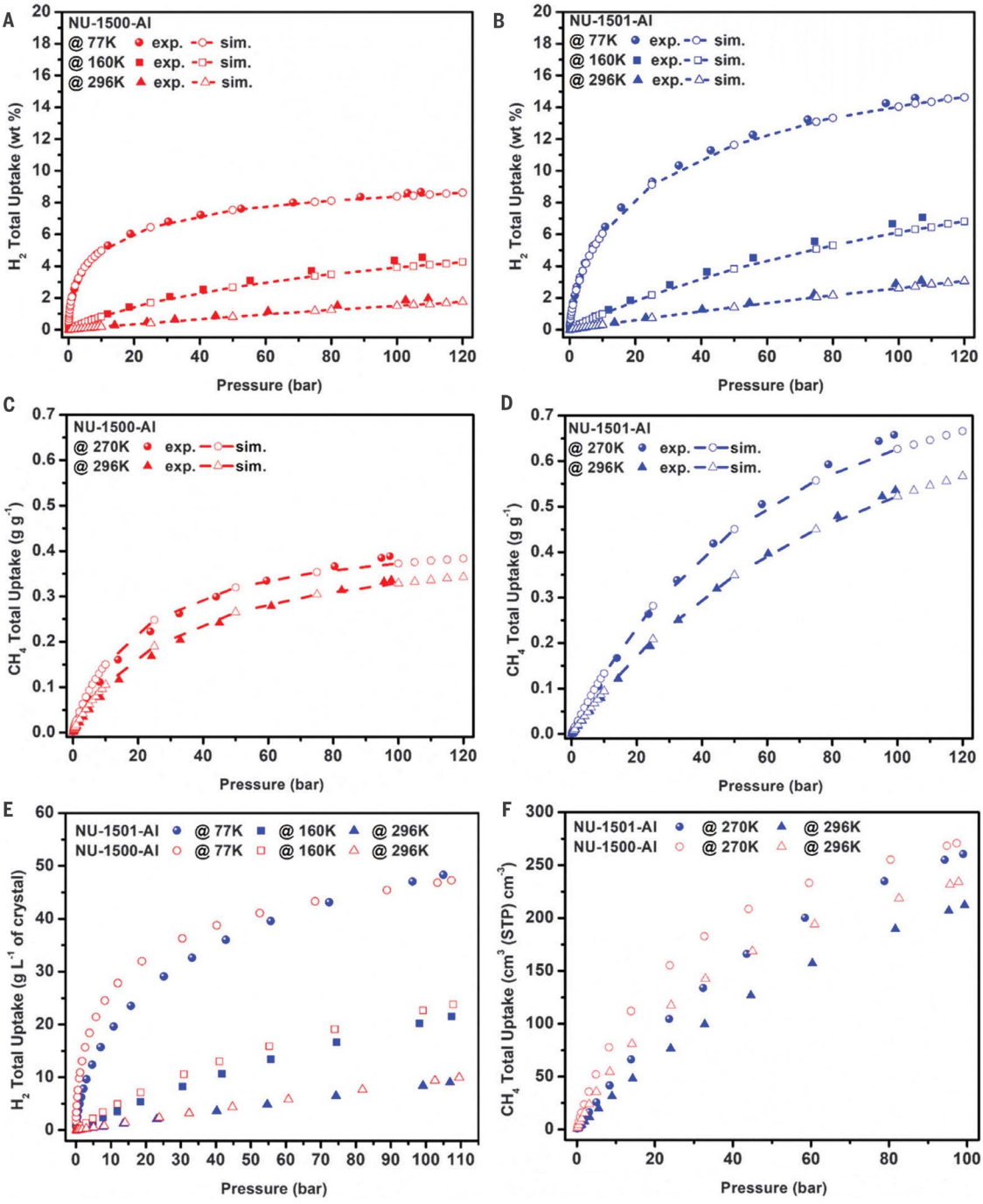

Fig. 4. High-pressure hydrogen and methane adsorption performance of NU-1500-Al and NU-1501-Al. (**A** and **B**) Experimental and simulated hydrogen adsorption uptake for NU-1501-Al and NU-1500-Al at 77, 160, and 296 K. (**C** and **D**) Experimental and simulated methane adsorption uptake for NU-1501-Al and NU-1500-Al at 270 and 296 K. In this work, the capacity (in wt %) of H_2 is calculated according to wt % = (mass of H_2)/(mass of H_2 + mass of MOF) × 100%. The dashed lines are a guide to the eye for simulated data. (**E** and **F**) Volumetric adsorption uptake of hydrogen and methane for NU-1501-Al and NU-1500-Al, calculated on the basis of crystallographic density.

gravimetric uptake of H_2 for NU-1501-Al at 100 bar and 296 K is ~2.9 wt % (volumetric uptake: 8.4 g liter^{-1}), which far exceeds the values of reported MOFs (generally between 1 and 2 wt % at 100 bar at room temperature) (*11*, *12*, *46*).

Additionally, the Q_{st} values from the H_2 adsorption isotherms at various temperatures indicated that NU-1501-Al exhibits small Q_{st} values of 4 and 2.6 kJ mol^{-1} at low and high loading, respectively. The Q_{st} for H_2 of NU-1501 at low loading is close to the enthalpy of adsorption from GCMC simulations at low pressure and slightly less than the Q_{st} of NU-1500-Al—i.e., 4.9 kJ mol^{-1} (table S9). These values indicate that the MOFs have modest host–guest interactions and that the large hydrogen capacities observed experimentally are driven by adsorbate–adsorbate interactions and the frameworks' substantial porosities. The combination of the experimentally obtained high-pressure hydrogen adsorption studies and GCMC molecular simulations demonstrate that the NU-1501 series are promising candidate materials for the onboard storage of hydrogen gas, owing to their ultrahigh gravimetric and volumetric surface areas and moderate pore volumes of ~2.90 cm^3 g^{-1} (in comparison to traditional ultraporous MOFs) that balance both volumetric and gravimetric capacity.

Conclusions

In conclusion, we have rationally designed and synthesized a class of ultraporous MOFs, NU-1501, with narrow mesoporosity which exhibit pore diameters of less than 2.5 nm. These

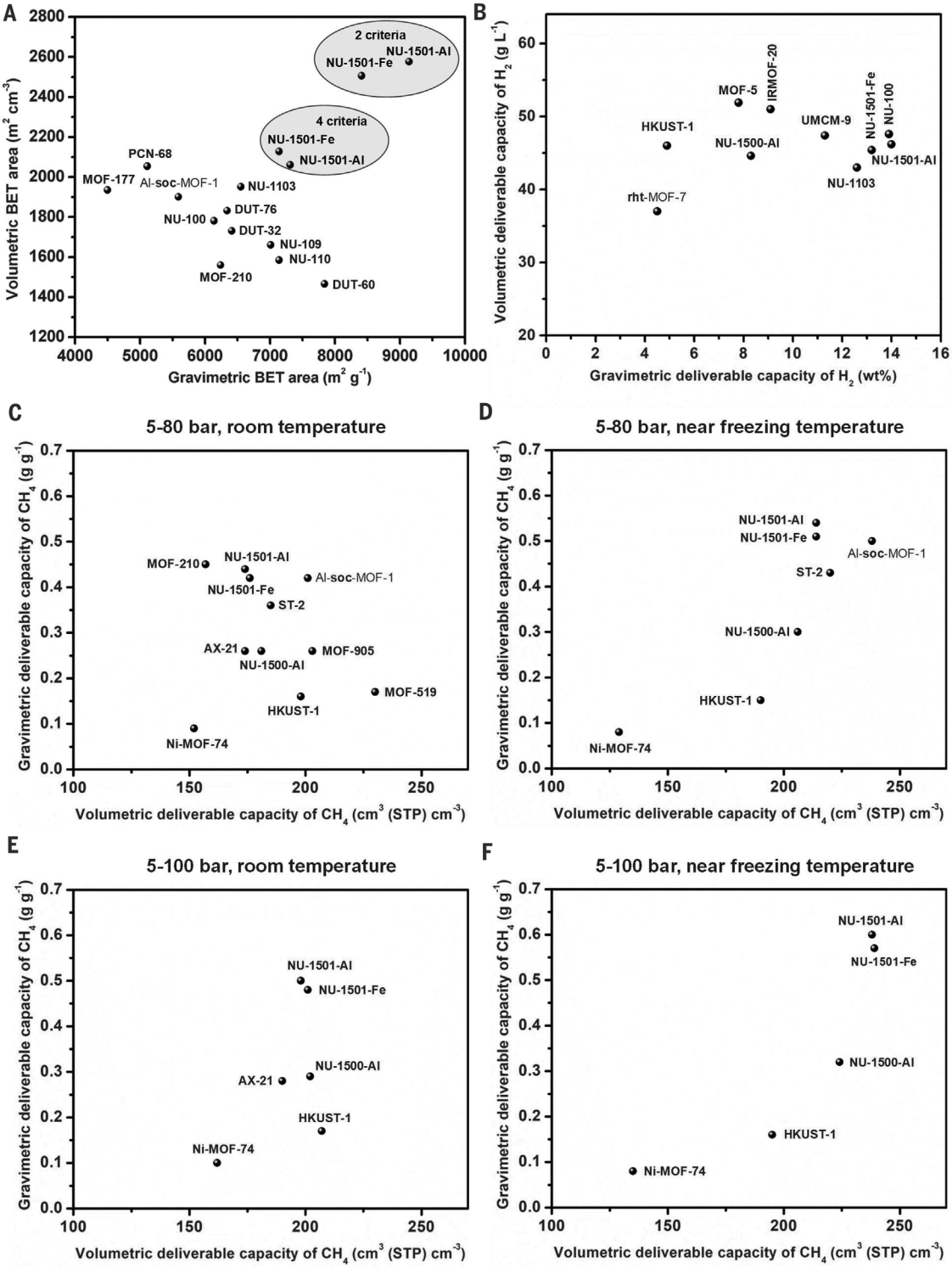

Fig. 5. Trade-offs of gravimetric and volumetric properties suggested by experimental adsorption studies. (**A**) Trade-off between gravimetric and volumetric BET area for selected ultrahigh porous materials. (**B**) Trade-off between gravimetric and volumetric deliverable hydrogen capacity under combined temperature and pressure swing conditions: 77 K/100 bar →160 K/5 bar. (**C** to **F**) Trade-off between gravimetric and volumetric deliverable methane capacity of MOFs for 5 to 80 bar and 5 to 100 bar at room temperature and near freezing temperature. Methane adsorption isotherms of MOFs in this work were performed at 296 and 270 K, and methane adsorption isotherms of other materials for comparison were performed at 298 and 273 K. For details of comparison, see tables S6 and S7 and figs. S28 to S30.

MOFs balance both gravimetric and volumetric BET areas, which make them ideal candidate adsorbent materials in onboard storage tanks for safe and effective storage of methane and hydrogen gases. In particular, NU-1501 has the highest apparent gravimetric BET areas among porous materials after satisfying all four BET consistency criteria. With a moderate pore volume compared to the conventional ultraporous materials such as MOF-210 (*7*), NU-110 (*28*), and DUT-60 (*30*), NU-1501 exhibits impressive volumetric BET areas. The combination of experiment and molecular simulation reveals that NU-1501 achieves outstanding gravimetric uptake, volumetric uptake, and deliverable capacities of methane and hydrogen simultaneously under practical operational conditions, making these materials a new class of promising MOF adsorbent candidates for the storage and delivery of methane and hydrogen—clean energy carriers related to the carbon-neutral energy system. Finally, the unambiguous structure-property relationship derived from the performance of this material, high-throughput computational

modeling, and experimental results will fuel the design and synthesis of the next generation of ultraporous sorbents for storage and delivery of clean fuel sources.

REFERENCES AND NOTES

1. U.S. Energy Information Administration (EIA), Monthly Energy Review, DOE/EIA-0035(2019/7), July 2019.
2. M. D. Allendorf *et al*., *Energy Environ. Sci.* **11**, 2784–2812 (2018).
3. A. Schoedel, Z. Ji, O. M. Yaghi, *Nat. Energy* **1**, 16034 (2016).
4. U.S. Energy Information Administration (EIA), Carbon Dioxide Emissions Coefficients (https://www.eia.gov/environment/emissions/co2_vol_mass.php), release date 2 February 2016.
5. J. A. Mason, M. Veenstra, J. R. Long, *Chem. Sci.* **5**, 32–51 (2014).
6. Y. Peng *et al*., *J. Am. Chem. Soc.* **135**, 11887–11894 (2013).
7. H. Furukawa *et al*., *Science* **329**, 424–428 (2010).
8. O. K. Farha *et al*., *Nat. Chem.* **2**, 944–948 (2010).
9. B. Li, H.-M. Wen, W. Zhou, J. Q. Xu, *Chem* **1**, 557–580 (2016).
10. M. Eddaoudi *et al*., *Science* **295**, 469–472 (2002).
11. D. Zhao, D. Yuan, H.-C. Zhou, *Energy Environ. Sci.* **1**, 222–235 (2008).
12. M. P. Suh, H. J. Park, T. K. Prasad, D.-W. Lim, *Chem. Rev.* **112**, 782–835 (2012).
13. D. Alezi *et al*., *J. Am. Chem. Soc.* **137**, 13308–13318 (2015).
14. M. T. Kapelewski *et al*., *Chem. Mater.* **30**, 8179–8189 (2018).
15. T. Tian *et al*., *Nat. Mater.* **17**, 174–179 (2018).
16. Y. Yan, S. Yang, A. J. Blake, M. Schröder, *Acc. Chem. Res.* **47**, 296–307 (2014).
17. K. V. Kumar, K. Preuss, M.-M. Titirici, F. Rodríguez-Reinoso, *Chem. Rev.* **117**, 1796–1825 (2017).
18. H. Furukawa, O. M. Yaghi, *J. Am. Chem. Soc.* **131**, 8875–8883 (2009).
19. D. Yuan, W. Lu, D. Zhao, H.-C. Zhou, *Adv. Mater.* **23**, 3723–3725 (2011).
20. J. Jia *et al*., *Chem* **5**, 180–191 (2019).
21. C. D. Wood *et al*., *Chem. Mater.* **19**, 2034–2048 (2007).
22. V. Rozyyev *et al*., *Nat. Energy* **4**, 604–611 (2019).
23. S. i. Noro, S. Kitagawa, M. Kondo, K. Seki, *Angew. Chem. Int. Ed.* **39**, 2081–2084 (2000).
24. P. L. Llewellyn *et al*., *Langmuir* **24**, 7245–7250 (2008).
25. J. Jiang, H. Furukawa, Y.-B. Zhang, O. M. Yaghi, *J. Am. Chem. Soc.* **138**, 10244–10251 (2016).
26. F. Gándara, H. Furukawa, S. Lee, O. M. Yaghi, *J. Am. Chem. Soc.* **136**, 5271–5274 (2014).
27. R. Grünker *et al*., *Chem. Commun.* **50**, 3450–3452 (2014).
28. O. K. Farha *et al*., *J. Am. Chem. Soc.* **134**, 15016–15021 (2012).
29. S. B. Kalidindi *et al*., *Angew. Chem. Int. Ed.* **54**, 221–226 (2015).
30. I. M. Hönicke *et al*., *Angew. Chem. Int. Ed.* **57**, 13780–13783 (2018).
31. D. J. Durbin, C. Malardier-Jugroot, *Int. J. Hydrogen Energy* **38**, 14595–14617 (2013).
32. Y. Peng *et al*., *Chem. Commun.* **49**, 2992–2994 (2013).
33. D. A. Gómez-Gualdrón *et al*., *ACS Appl. Mater. Interfaces* **9**, 33419–33428 (2017).
34. A. Ahmed *et al*., *Energy Environ. Sci.* **10**, 2459–2471 (2017).
35. S. S.-Y. Chui, S. M.-F. Lo, J. P. H. Charmant, A. G. Orpen, I. D. Williams, *Science* **283**, 1148–1150 (1999).
36. Z. Chen *et al*., *J. Am. Chem. Soc.* **141**, 2900–2905 (2019).
37. P. Li *et al*., *Angew. Chem. Int. Ed.* **58**, 1664–1669 (2019).
38. T. Devic, C. Serre, *Chem. Soc. Rev.* **43**, 6097–6115 (2014).
39. P. Llewellyn, F. Rodriguez-Reinoso, J. Rouquerol, N. Seaton, "Characterization of Porous Solids VII" in *Studies in Surface Science and Catalysis*, Eds. (Elsevier, 2007), vol. 160, pp. 49–56.
40. D. A. Gómez-Gualdrón, P. Z. Moghadam, J. T. Hupp, O. K. Farha, R. Q. Snurr, *J. Am. Chem. Soc.* **138**, 215–224 (2016).
41. P. García-Holley *et al*., *ACS Energy Lett.* **3**, 748–754 (2018).
42. Y. J. Colón, D. A. Gómez-Gualdrón, R. Q. Snurr, *Cryst. Growth Des.* **17**, 5801–5810 (2017).
43. Z. Chen *et al*., *J. Am. Chem. Soc.* **141**, 12229–12235 (2019).
44. C.-C. Liang *et al*., *J. Am. Chem. Soc.* **139**, 13300–13303 (2017).
45. A. Ahmed *et al*., *Nat. Commun.* **10**, 1568 (2019).
46. K. Sumida, M. R. Hill, S. Horike, A. Dailly, J. R. Long, *J. Am. Chem. Soc.* **131**, 15120–15121 (2009).
47. B. J. Bucior *et al*., *Cryst. Growth Des.* **19**, 6682–6697 (2019).

ACKNOWLEDGMENTS

Funding: O.K.F. gratefully acknowledges research support from the U.S. Department of Energy's Office of Energy Efficiency and Renewable Energy (EERE) under award no. DE-EE0008816. P.L. and J.F.S. acknowledge the Joint Center of Excellence in Integrated Nano-Systems (JCIN) at King Abdulaziz City for Science and Technology (KACST) and Northwestern University (NU). D.A.G-G. acknowledges funding from NSF CAREER (award CBET 1846707). Simulations were performed at the Mio supercomputer cluster maintained by the Colorado School of Mines. L.R.'s contribution to this work is based on work supported by the U.S. Department of Energy (DOE), Office of Science, Office of Workforce Development for Teachers and Scientists, Office of Science Graduate Student Research (SCGSR) program. The SCGSR program is administered by the Oak Ridge Institute for Science and Education (ORISE) for the DOE. ORISE is managed by ORAU under contract DE-SC0014664. This work made use of the EPIC facility of Northwestern University's NU*ANCE* Center, which has received support from the Soft and Hybrid Nanotechnology Experimental (SHyNE) Resource (NSF ECCS-1542205); the MRSEC program (NSF DMR-1720139) at the Materials Research Center; the International Institute for Nanotechnology (IIN); the Keck Foundation; and the State of Illinois, through the IIN. This work made use of the IMSERC at Northwestern University, which has received support from the Soft and Hybrid Nanotechnology Experimental (SHyNE) Resource (NSF ECCS-1542205), the State of Illinois, and the International Institute for Nanotechnology (IIN).
Author contributions: O.K.F. supervised the project; Z.C. and O.K.F. conceived and designed the experiments; P.L. synthesized the ligand under the supervision of J.F.S.; Z.C. synthesized MOF materials; R.A. conducted molecular simulation under the supervision of D.A.G.; X.W. and Z.C. performed activation and low-pressure sorption in Northwestern University; Z.C. collected and analyzed the single-crystal data with help from X.Z.; Z.C. characterized MOF materials with help from X.W., L.R., L.R.R., S.M., and T.I.; T.Y. conducted the low-pressure and high-pressure sorption studies at NIST with the samples sent from Northwestern University; Z.C. analyzed low-pressure and high-pressure sorption data with help from O.K.F., R.A., D.A.G., and T.Y.; Z.C., L.R., and O.K.F. wrote the manuscript, and all authors commented and revised on the manuscript. **Competing interests:** O.K.F. has a financial interest in NuMat Technologies, a startup company that is seeking to commercialize MOFs. **Data and materials availability:** The x-ray crystallographic data for NU-1501-Al and NU-1501-Fe have been deposited at the Cambridge Crystallographic Data Centre (CCDC), under deposition no. CCDC 1909853, 1909854, and 1945113. These data can be obtained free of charge from the CCDC via www.ccdc.cam.ac.uk. Crystallographic information for NU-1501-Al and NU-1501-Fe can also be found in the supplementary data. MOFkey (*47*): Al.PZUNVLJATCTESM.MOFkey-v1.acs (NU-1500-Al), Fe.GKGWJFNTVGTMJR.MOFkey-v1.acs (NU-1501-Fe), Al.GKGWJFNTVGTMJR.MOFkey-v1.acs (NU-1501-Al). All other relevant data supporting the findings of this study are presented in the paper or the supplementary materials.

SUPPLEMENTARY MATERIALS

science.sciencemag.org/content/368/6488/297/suppl/DC1
Materials and Methods
Supplementary Text
Figs. S1 to S54
Tables S1 to S10
Captions for Data S1 to S3
References (*48*–*83*)
Data S1 to S3

17 October 2019; accepted 17 March 2020
10.1126/science.aaz8881

Science

Balancing volumetric and gravimetric uptake in highly porous materials for clean energy

Zhijie ChenPenghao LiRyther AndersonXingjie WangXuan ZhangLee RobisonLouis R. RedfernShinya MoribeTimur IslamogluDiego A. Gómez-GualdrónTaner YildirimJ. Fraser StoddartOmar K. Farha

Science, 368 (6488), • DOI: 10.1126/science.aaz8881

Delivering methane and hydrogen

The pressure for onboard storage of methane and hydrogen on vehicles is usually limited to 100 bar for the use of lightweight containers, but the amount stored can be increased with the use of absorbent materials. Efficient storage and delivery require a balance of volumetric and gravimetric storage. Chen *et al.* designed a metal-organic framework with trialuminum nodes and a large hexadentate aromatic linker that optimizes both parameters. This material surpassed the U.S. Department of Energy targets for methane and had a deliverable capacity of 14% by weight for hydrogen.

Science, this issue p. 297

Science (ISSN 1095-9203) is published by the American Association for the Advancement of Science. 1200 New York Avenue NW, Washington, DC 20005. The title *Science* is a registered trademark of AAAS.